Journal of Materials Chemistry A

ROYAL SOCIETY OF CHEMISTRY

PAPER

View Article Online
View Journal | View Issue

Cite this: J. Mater. Chem. A, 2025, 13, 19623

Facet-dependent photocatalytic reduction of nitroaromatics using tailored $SrTiO_3$ crystals: mechanism and reactivity enhancement†

Wiktoria Adamowicz, [ab] Wojciech Macyk [a] and Marcin Kobielusz *[a]

This work presents a selective photocatalytic reduction of nitroaromatics to amines on tailored $SrTiO_3$ crystals. Exploring the role of exposed facets reveals their substantial impact on both the efficiency and selectivity of this type of reduction reaction. A series of uniform $SrTiO_3$ crystals with systematically varied morphologies, differing only in shape and type of exposed facets, were synthesised. Photoelectrochemical measurements and photodeposition experiments demonstrated that reduction reactions preferentially occur on the {001} facets, while oxidation predominantly takes place on the {110} facets. Furthermore, the {110} facets play a key role in enhancing charge separation, thereby significantly boosting photocatalytic activity. The changes in the efficiency of photocatalytic oxidation of terephthalic acid follow the same pattern as photocurrent generation. Using tailored $SrTiO_3$ crystals, the reduction of nitroaromatic compounds was achieved with outstanding conversion rates (up to 40 times higher compared to commercial $SrTiO_3$). Although {110} facets facilitate charge separation, transforming nitroaromatics to amines requires {001} planes.

Received 3rd March 2025
Accepted 27th April 2025

DOI: 10.1039/d5ta01766a

rsc.li/materials-a

Introduction

Using photocatalysis in organic synthesis has emerged as a promising alternative to traditional methods, which often generate significant amounts of waste. Among these, the photocatalytic selective reduction of nitroaromatic compounds stands out as an environmentally friendly approach.[1,2] This reaction has been demonstrated to achieve high, nearly 100% selectivity in the presence of TiO_2.[3–5] Alcohol solutions play a crucial role in the photocatalytic reduction of nitroaromatics by scavenging hydroxyl radicals, which otherwise contribute to undesired side reactions. This underscores the potential of employing photocatalysts that minimise hydroxyl radical generation by favouring alternative oxidation pathways, leading to the formation of weaker oxidants, such as oxygen.

Perovskite-type $SrTiO_3$ is one of the most extensively studied photocatalysts for water splitting due to its suitable electronic band structure, anisotropic crystal facets, efficient separation and transport of photogenerated charge carriers, low cost, and high resistance to photocorrosion in aqueous conditions.[6–13] An $SrTiO_3$-based photocatalyst recently demonstrated a remarkable quantum efficiency of 93% at 365 nm for water splitting, as reported by Domen *et al.*[14]

These properties of $SrTiO_3$, including its ability to oxidise water to mild oxidants like oxygen, make this material particularly interesting for applications in the reduction of nitroaromatics. Moreover, this material offers a lower conduction band edge potential compared to anatase-TiO_2, which has previously been tested in these reactions.[15] Although there are reports of its use as a thermal catalyst for reducing nitroaromatics,[16] to the best of our knowledge, it has not been tested in this reaction as a photocatalyst so far. Among similar titanates, only $CaTiO_3$ has been reported as a photocatalyst in the conversion of nitrobenzene to aniline.[17] Our preliminary studies reveal that while $BaTiO_3$, $CaTiO_3$, and $SrTiO_3$ can all photocatalytically reduce nitroaromatic compounds, $SrTiO_3$ exhibits significantly higher activity, despite only modest differences in other tests, such as photocurrent measurements (Fig. S1†).

The physical and chemical properties of nanocrystals are influenced not only by their size, specific surface area, crystallinity and crystal structure but also by the type of exposed facets.[18–20] Polyhedral nanocrystals with well-defined facets, synthesised under the same conditions, are an outstanding area for investigating how material properties vary with specific crystal facets. Exposed facets of $SrTiO_3$ are characterised by distinct atomic configurations and electronic structures and play a pivotal role in governing surface reactions and overall material activity.[6] Therefore, the influence of $SrTiO_3$ exposed facets remains a topic of ongoing research.

[a]Faculty of Chemistry, Jagiellonian University, ul. Gronostajowa 2, 30-387 Kraków, Poland. E-mail: kobielusz@chemia.uj.edu.pl

[b]Doctoral School of Exact and Natural Sciences, Jagiellonian University, ul. Łojasiewicza 11, 30-348 Kraków, Poland

† Electronic supplementary information (ESI) available. See DOI: https://doi.org/10.1039/d5ta01766a

There are various methods to synthesise and control the formation of exposed facets of strontium titanate, such as the hydrothermal method using a series of alcohols[21–23] or the solvothermal method, tuning sodium hydroxide and ethanolamine concentrations.[24,25] The properties of tailored $SrTiO_3$ crystals have been studied in many different reactions such as water splitting,[14,22,26,27] CO_2 reduction,[28] ethanol dehydrogenation,[29] isopropanol conversion,[30] hydrogen or oxygen evolution,[24,31–35] and dye photodegradation.[31,33,36] Other tests, such as electrical conductivity measurements or the influence of light intensity, were also conducted to explain the differences in the properties of the exposed facets of this material.[37,38] The results of all studies indicate increased activity of tailored $SrTiO_3$ crystals and differences in the activity of $SrTiO_3$ crystals depending on the type of exposed facets or the ratio between exposed facets. Polyhedral $SrTiO_3$ exposing multiple facets, including {100}, {110}, and {111}, demonstrates improved photocatalytic activity compared to those exposing only the {100} facet.[23,27] In particular, the combination of {100} facets, which facilitate electron transfer due to their lower work function, and Sr-rich {110} facets, promoting efficient charge separation, contributes significantly to the enhanced photocatalytic performance.[34,39,40]

The study aims to clarify the influence of exposed facets of $SrTiO_3$ crystals on the efficiency and selectivity of reduction of nitrobenzene derivatives and to identify factors contributing to the rates of these reactions.

Experimental

Synthesis of tailored $SrTiO_3$ crystals

A series of tailored $SrTiO_3$ crystals was performed by hydrothermal synthesis with different types and amounts of alcohol (5 cm^3 of methanol, 1.8 cm^3 of ethylene glycol or 2 cm^3 of propylene glycol). In a typical synthesis, 0.45 cm^3 of $TiCl_4$ was added dropwise into 50 cm^3 of deionised water containing appropriate alcohol cooled in an ice bath. Exceptionally, for cube-shaped crystals, the amount of $TiCl_4$ was 0.42 cm^3. After stirring for 5 minutes, 60 cm^3 of 3 mol dm^{-3} LiOH solution was added, and then after 5 minutes of stirring, 20 cm^3 of 0.24 mol dm^{-3} $SrCl_2$ was added. After stirring for another 30 minutes, the solution was transferred to a 200 cm^3 Teflon-lined stainless steel autoclave and heated at 180 °C for 60 or 72 h. Then, the autoclave was cooled to room temperature under ambient conditions, and the resulting residue was centrifuged. The synthesised crystals were washed with methanol and water five times, then dried at 40 °C for 12 h. As a result of the synthesis, cubic $SrTiO_3$ crystals with identical 6 facets exposed and 18-facet $SrTiO_3$ crystals with two different types of exposed facets were obtained. To distinguish the synthesized materials, the crystals were named accordingly: cubes, slightly truncated cubes, truncated cubes, and truncated rhombic dodecahedrons.

Materials characterisation

Micrographs of synthesised materials (cubes, slightly truncated cubes, truncated cubes, and truncated rhombic dodecahedrons) were taken by scanning electron microscopy (SEM Helios 5 Hydra DualBeam, immersion mode), equipped with the EDS detector (EDAX Octane Elite). The measurements were performed on carbon tape. The average particle size was calculated based on SEM images.

The crystalline structure of synthesised materials was studied by powder X-ray diffraction (XRD) using a Rigaku MiniFlex 600 X-ray diffractometer. The Cu K_α radiation (0.3 mm filter) in a 2θ degree range of 20–80°, with a scan rate of 3° per min and the scan step of 0.02° was applied. In order to determine the changes in the fraction of {110} facets, the ratio of the intensity of (220) to (200) peak was calculated from diffractograms.

Nitrogen adsorption–desorption isotherms were measured at 77 K using an automated gas sorption analyser (Autosorb iQ, Quantachrome Instruments). The Brunauer–Emmett–Teller model was used to calculate specific surface areas of the samples.

Spectroscopic analysis

The diffuse reflectance spectra of tailored $SrTiO_3$ samples were measured using a UV-Vis-NIR spectrophotometer (Shimadzu, UV-3600i Plus) equipped with a 6 cm integrating sphere in the 200–950 nm spectral range. Each sample was ground with barium sulfate. The collected reflectance spectra were transformed to the Kubelka–Munk function, and then, to determine the band gap energies, the Tauc transformation was applied.[41]

Photodeposition of Ag and Co_3O_4

Photodeposition of 5 wt% Ag and Co_3O_4 on the surface of $SrTiO_3$ was carried out using $AgNO_3$ and $Co(NO_3)_2$. 4 mg of $SrTiO_3$ (cubes and truncated rhombic dodecahedrons) was added to the solution of $AgNO_3$ (0.46 mmol dm^{-3}) or $Co(NO_3)_2$ (0.67 mmol dm^{-3}). Additionally, KIO_3 (20 mg cm^{-3}) was used as the electron acceptor during photodeposition of Co_3O_4. Under constant stirring, the suspension was irradiated with an XBO-150 xenon lamp (Instytut Fotonowy). After 2 hours of reaction, the suspension was washed with deionised water and methanol five times and dried at 40 °C for 12 h.

Photoelectrochemical measurements

Photoelectrochemical measurements were performed using Instytut Fotonowy potentiostat in a three-electrode setup with light supplied by a 150 W Xe lamp (XBO-150) passing through a monochromator. The working electrode was made of a thin sample layer placed on ITO-coated transparent foil (60 Ω per sq resistance, Sigma Aldrich). The counter electrode was a platinum wire, and the reference electrode was an Ag/AgCl electrode in a 3 mol dm^{-3} KCl solution. The electrolyte, 0.1 mol dm^{-3} KNO_3 aqueous solution, was purged with argon for 15 minutes before the beginning until the end of each experiment. The working electrodes were irradiated in the spectral range of 330–500 nm, with 0.1 V steps of the potential applied in the range of −0.2 to 1.0 V *vs.* Ag/AgCl. The photocurrent doubling effect was studied in the presence of methanol (a sacrificial agent, concentration of 6.5%).

Photocatalytic activity

The photocatalytic activity of the materials was studied in the reactions of terephthalic acid (TA) hydroxylation and reduction of nitroaromatic compounds. The reaction mixture for tests with hydroxyl radical generation was prepared according to the following procedure. $SrTiO_3$ (1.0 g dm^{-3}) was suspended in 16 cm^3 of the 0.3 mmol dm^{-3} terephthalic acid solution. The prepared suspension was placed in a round quartz cuvette (16 cm^3 volume) and irradiated with an XBO-150 xenon lamp (Instytut Fotonowy) for 1 h under constant stirring. Additionally, an IR filter (0.1 mol dm^{-3} $CuSO_4$ aqueous solution, 10 cm optical path) and a 320 nm cut-off filter were used. For each filtered (0.22 μm MCE filter) and centrifuged sample (2 cm^3), the concentration of generated hydroxyl radicals was determined by emission spectroscopy. As a result of the reaction, fluorescent hydroxyterephthalic acid (TAOH) with a broad emission band at $\lambda_{max} = 426$ nm (when excited $\lambda_{max} = 315$ nm) was recorded.

Reduction of nitroaromatics was tested in $SrTiO_3$ suspensions in a 50 : 50 mixture of water and methanol (0.5 g dm^{-3}), always sonicated for 5 minutes under the same conditions (generator: 3 × 80 W; frequency of the sonication: approx. 37 kHz). The suspension was mixed with 3-nitrophenol (3-NP), 1-iodo-4-nitrobenzene (INB) or 4-nitrobenzoic acid (PNBA) with the final nitroaromatics concentration of 0.3 mmol dm^{-3}. The prepared suspension was placed in a round quartz cuvette (16 cm^3), purged with argon for 15 minutes and then irradiated for 2 h under constant stirring, using the same setup as in TA hydroxylation tests. For each filtered (0.22 μm MCE filter) and centrifuged sample, the concentration of reagents in the collected samples (2 cm^3) was determined by HPLC (Shimadzu Prominence-i LC-2030 3D) with a Poroshell 120 SB-C18 column (3.0 × 100 mm, 2.7 μm) and detected at 246, 266, 272, 283, 297 and 332 nm using a photodiode array detector. The mobile phase was a mixture of methanol and water (50 : 50) with a flow rate of 0.4 mL min^{-1}. The reaction rate constant (assuming the first-order kinetics) was determined by calculating the natural logarithm of the product concentration at the time of irradiation and plotting the product increment against time. The slope of the linear fitting of the plot gives the reaction rate constant.

The reduction reactions were carried out in optimal water : methanol 1 : 1 mixture based on our previous experience. Methanol has three roles: (i) a solvent for nitroaromatic compounds, (ii) a hole scavenger and (iii) an additional electron donor for an efficient transformation. As the methanol content increases to a ratio of 1 : 1, the conversion rate steadily increases. However, a further increase in the methanol content decreases the reaction rate.[42] This behaviour was verified for cubes and truncated rhombic dodecahedrons in the reduction of 4-nitrobenzoic acid in water (Fig. S2†). Reduction reactions in the absence of methanol practically do not occur.

Results and discussion

All the synthesised strontium titanate materials were obtained in the form of white powders. The morphology of a series of the synthesised $SrTiO_3$ crystals with systematic shape evolution was confirmed using SEM (Fig. 1). The inner images show single crystals with the labelled exposed facets. Cube-shaped crystals obtained in synthesis with methanol have only the {001} type of exposed facets. Lowering pK_a of the alcohol used in the reaction medium (propylene glycol instead of methanol) resulted in truncated cubes with a second type of the exposed facet, {110}.

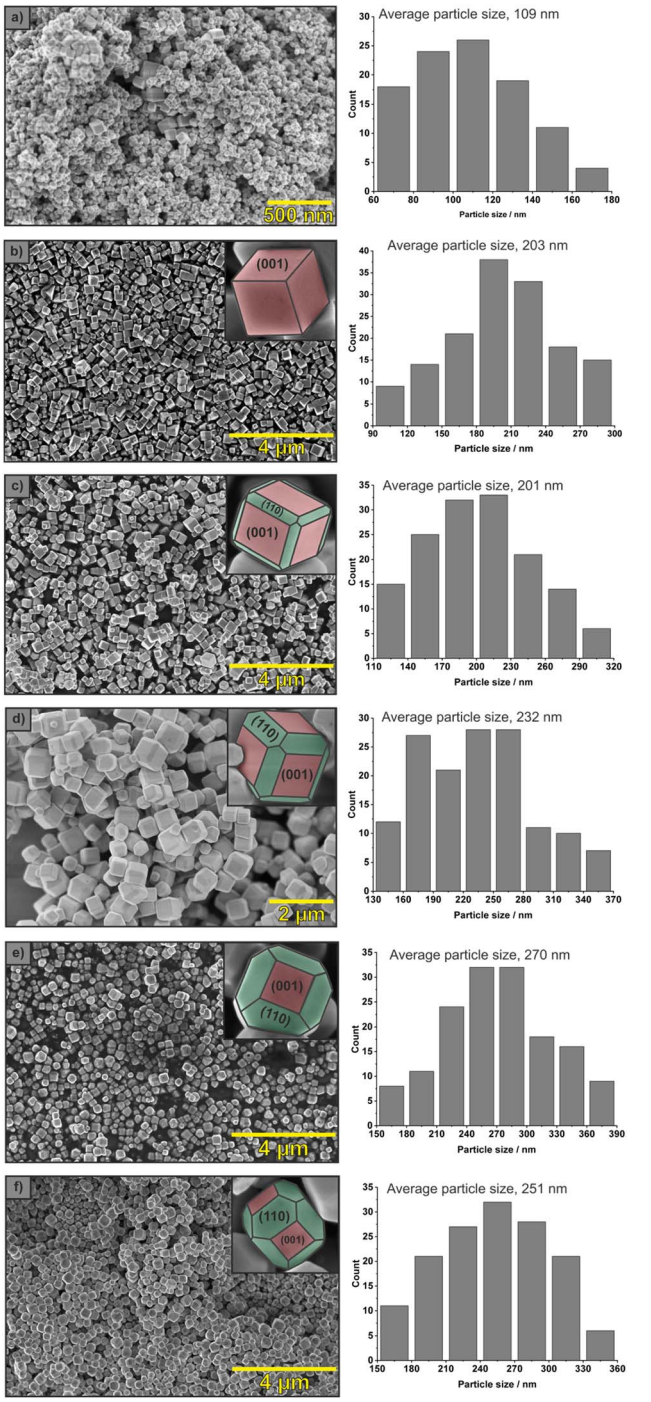

Fig. 1 SEM images and size distribution of strontium titanate crystals in different shapes – commercial reference sample (a), cubes (b), slightly truncated cubes (c), truncated cubes (d), rhombic dodecahedrons synthesised with propylene glycol (e) and rhombic dodecahedrons synthesised with ethylene glycol (f).

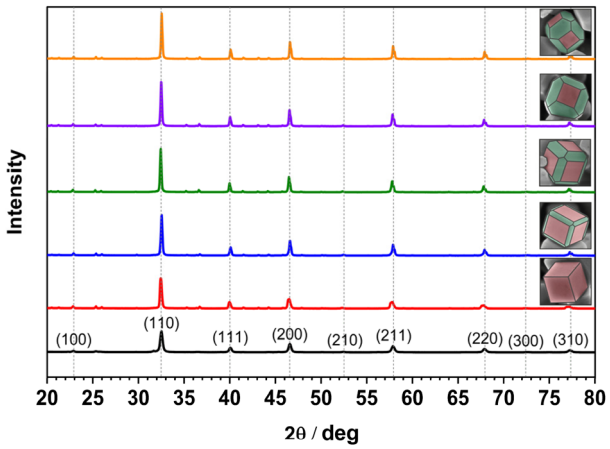

Fig. 2 XRD patterns of tailored strontium titanate in the shape of cubes, slightly truncated cubes, truncated cubes and rhombic dodecahedrons. The black line represents commercial $SrTiO_3$.

Using alcohol with even lower pK_a (ethylene glycol) led to truncated rhombic dodecahedron-shape crystals with the predominantly exposed {110} facets. Nanocrystals are uniform, without impurities and exhibit comparable crystal sizes of about 200–270 nm compared to the small, irregular commercial $SrTiO_3$ crystals. Consequently, the specific surface area of the euhedral $SrTiO_3$ crystals is similar for the whole series, *ca.* three times smaller than the commercial sample.

XRD patterns of the synthesised crystals are shown in Fig. 2. Only strontium titanate characteristic peaks are present, and the peak positions are the same for all materials. The peak intensity ratio, $I_{(220)}/I_{(200)}$, increases with the shape evolution from 0.35 for cubes to 0.43 for truncated rhombic dodecahedrons (Table 1). This trend is related to the increasing contribution of {110} facet. Additionally, EDS spectra were collected for cubes and truncated rhombic dodecahedrons (Fig. S3†). They confirm that on the surface of the crystals, there are no residues of precursors, such as chloride ions, that could affect the photoactivity of these materials.

The band gap energy values were determined based on DRS spectra. The Tauc plots for the samples are presented in Fig. S4.† The calculated band gap energy values are the same, within the error, for the entire series (Table 1). Only the commercial strontium titanate reference sample has a lower band gap energy. The physicochemical characterisation indicates that the series of obtained strontium titanate crystals differ only in morphology and exposed facets. Neither the light absorption abilities nor the BET surface area of these samples rationalise differences in their photocatalytic activity (*vide infra*).

To verify the dependence of charge separation efficiency on crystal shape photocurrent measurements were performed. The photocurrent intensity is closely related to the effectiveness of photoinduced charge separation. Various photocurrent generation efficiencies are observed for various materials under comparable conditions, *i.e.*, the same applied potential and incident light intensity (Fig. 3). Increasing the contribution of {110} facets results in higher photocurrents. Importantly, not only are the photocurrent intensities enhanced for truncated rhombic dodecahedrons in comparison to cubic crystals, but also the decay time of the photocurrent signals is prolonged, as clearly illustrated in the transient photocurrent response shown in Fig. S5† and its normalized form. This slower decay indicates reduced recombination rates of photogenerated charge carriers. The presence of two types of facets (the so-called homojunction) can result in a selective transfer of electrons and holes to

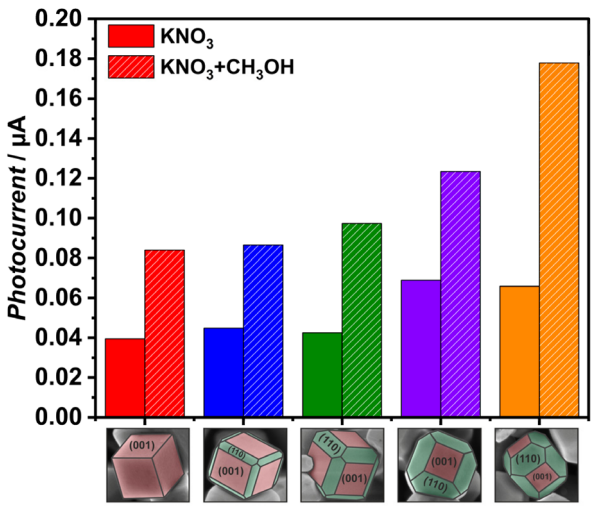

Fig. 3 Photocurrents generated by various $SrTiO_3$ crystals. The measurements were carried out with and without methanol.

Table 1 Comparison of XRD intensities, specific surface area, average particle size and band gap energy of tailored $SrTiO_3$ crystals

$SrTiO_3$ shapes	Foremost exposed facets	$I_{(220)}/I_{(200)}$	$L_{\{110\}}/L_{\{100\}}$	Specific surface area [$m^2\ g^{-1}$] ± 2%	Average particle size [nm]	Band gap energy [eV] ± 0.01 eV
Commercial	—	0.40	—	29.6	109	3.19
Cubes	{001}	0.35	—	9.7	203	3.25
Slightly truncated cubes	{001}	0.39	0.3 ± 0.1	8.8	201	3.22
Truncated cubes	{001} and {110}	0.39	0.4 ± 0.2	11.3	232	3.24
Truncated rhombic dodecahedron (propylene glycol)	{110}	0.40	0.6 ± 0.3	11.0	270	3.24
Truncated rhombic dodecahedron (ethylene glycol)	{110}	0.43	0.7 ± 0.2	8.2	251	3.23

different facets, *i.e.* {001} and {110}, respectively,[27,31] and thus better charge separation efficiency.

Methanol can play a dual role in increasing photocurrent – it can act as an efficient hole scavenger and the so-called photocurrent doubling agent, which, upon oxidation with a hole to the short-living radical ($^{\bullet}CH_2OH$), may deliver another electron to the conduction band.[43] Such an effect, which should result in at least a doubling of photocurrent, was observed for all synthesised tailored $SrTiO_3$ materials. The highest photocurrent and photocurrent multiplication factor observed for truncated rhombic dodecahedrons with a higher surface of {110} may indicate the importance of {110} facet in oxidation reactions (Fig. 3).

The enhanced photocurrent generation efficiency with an increased fraction of the {110} facets can be attributed to improved charge separation facilitated by the spatial segregation of charges on the surface. Studies have shown that the degree of upward band bending varies with the type of crystal facet, influencing the localised accumulation of specific photogenerated charge carriers.[7,26,31,37,44] This phenomenon can lead to regions being enriched in photogenerated holes and others in photogenerated electrons. Consequently, these distinct regions may act as preferred sites for reduction and oxidation reactions. Jia *et al.*, while investigating this phenomenon for $SrTiO_3$, demonstrated that charge separation is more efficient for materials with an $L_{\{110\}}/L_{\{100\}}$ facet ratio of 1, compared to those with a ratio of 0.2.[39] In our case, the highest photoelectrochemical activity is observed for materials with facet ratios of 0.6 and 0.7 (Table 1), which is in good agreement with their observations.

Photodepositions of silver and cobalt(III) oxide were performed on cubic and truncated rhombic dodecahedral $SrTiO_3$ crystals to test whether reduction and oxidation reactions occur preferentially on different exposed facets. Fig. 4 shows SEM images before and after the photoreduction- and photooxidation-based deposition. Additionally, EDS maps were collected to verify the deposition of Ag and Co_2O_3 (Fig. S6†). For cubes with only one available exposed facet, {001}, silver and cobalt(III) oxide are deposited on every facet of the $SrTiO_3$ crystal without any preference. Remarkably, for truncated rhombic dodecahedron $SrTiO_3$ crystals, it was found that silver deposited mainly on the {001} facet (Fig. 4e), while cobalt(III) oxide deposited almost exclusively on the {110} facet (Fig. 4f). These results are consistent with observations obtained from photocurrent measurements and indicate that in the presence of two different exposed facets, oxidation reactions occur preferentially on the {110} surface. In contrast, reduction reactions occur preferentially on the {001} surface of the $SrTiO_3$ crystals. The presence of only one type of exposed facet does not inhibit the reaction, and both oxidation and reduction reactions proceed. These findings are entirely consistent with previous reports.[22] Based on our results, it can be concluded that the photogenerated electrons and holes are distributed on all {001} facets of cubic $SrTiO_3$, while for truncated rhombic dodecahedral $SrTiO_3$, electrons and holes are accumulated on {001} and {110} facets, respectively.

A photocatalytic hydroxylation test of terephthalic acid was conducted to understand better the effect of faceted $SrTiO_3$ on the reduction of nitroaromatics. The hydroxylation of terephthalic acid to highly fluorescent hydroxyterephthalic acid is a selective reaction used to measure the efficiency of photocatalytic hydroxyl radicals generation.[45] Strontium titanate, while more readily oxidising water to oxygen than TiO_2, is still capable of directly oxidising water and reducing molecular oxygen to hydroxyl radicals through a three-step mechanism.[46] Combined with photocurrent studies, these tests should enable an assessment of the general relationship between photocatalytic activity and the material type. For various materials with predominantly exposed {001} facets, the efficiency of hydroxyl radicals generation was almost identical (Fig. 5). For truncated rhombic dodecahedrons with predominant oxidative {110} facets, the photocatalytic activity was higher. Changes in photocatalytic activity follow the same pattern as photocurrent generation (compare Fig. 4 and 5). This coincidence shows that despite using an external potential, photocurrent efficiency

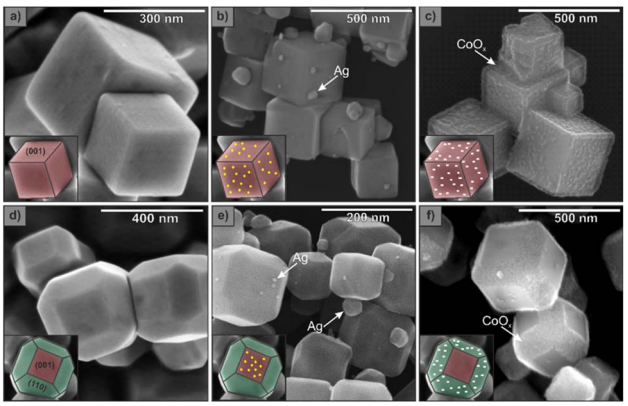

Fig. 4 The SEM images of the $SrTiO_3$ cubes and rhombic dodecahedrons with photodeposited silver or cobalt(III) oxide. Cubic $SrTiO_3$ crystals before photodeposition (a), loaded with Ag (b) and Co_2O_3 (c). Rhombic dodecahedrons of $SrTiO_3$ before photodeposition (d), loaded with Ag (e) and Co_2O_3 (f).

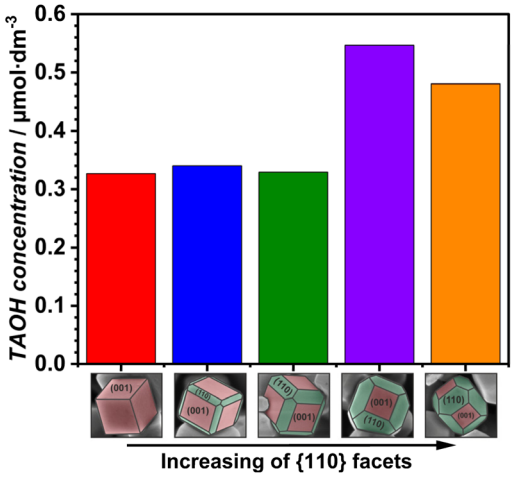

Fig. 5 Concentration of TAOH photogenerated in the photocatalytic oxidation of TA in the presence of tailored $SrTiO_3$ crystals after 30 minutes of irradiation.

directly translates to photocatalytic activity. Moreover, this further confirms more efficient charge separation for truncated rhombic dodecahedrons in which both exposed facets, {110} and {001}, are present. Noteworthy, the Sr-rich termination of the {110} facet provides active sites that facilitate hydroxyl radical generation by promoting the adsorption and activation of water molecules,[47] which may also contribute to the observed enhancement in photocatalytic performance.

The photocatalytic activity of the synthesised $SrTiO_3$ crystals was evaluated by reducing three different nitrobenzene derivatives: 3-nitrophenol, 1-iodo-4-nitrobenzene, and 4-nitrobenzoic acid. These reactions were carried out in a 1 : 1 water/methanol mixture, yielding the corresponding aniline derivatives: 3-aminophenol (3-AP), 4-iodoaniline (IA), and 4-aminobenzoic acid (PABA) (Fig. S7†). The selected substrates and their reduction products were confirmed to be stable and photostable under the experimental conditions. The selected nitroaromatic compounds have diverse functional groups with different substituent effects, which affect the reducibility of these compounds. The hydroxyl group in 3-nitrophenol belongs to the electron-donating groups (EDG). Donating electron density to the aromatic ring makes the nitro group less electrophilic and – in general – harder to reduce.[48] The carboxyl group in 4-nitrobenzoic acid is an electron-withdrawing group (EWG). It lowers the electron density on the nitro group and thereby stabilises the transition state, making the reduction process more favourable.[48,49] Iodine is qualified as a weak electron-withdrawing group, but the selective reduction of the nitro group may be hindered by iodine susceptibility to its abstraction from the aromatic ring.[50] Using different functionalities (both electron-withdrawing and electron-donating) allows for more general conclusions on the influence of the available $SrTiO_3$ facets on their photoactivity in reducing nitrobenzene derivatives.

The rate constant for reducing selected nitroaromatics increases for all materials in the order INB < 3NP < PNBA (Fig. 6), independently of the exposed facets. It is consistent with expectations based on the electronic effects of substituents (EWG/EDG). Hence, the most easily reduced compound is 4-nitrobenzoic acid. Truncated cubes and rhombic dodecahedrons with $I_{(220)}/I_{(200)} = 0.40$ (Table 1) appeared to be the most active materials. Also, these types of tailored $SrTiO_3$ crystals exhibit higher reaction rate constants than commercial $SrTiO_3$, although the specific surface area is three times smaller. Noteworthy, for truncated cubes and truncated rhombic dodecahedrons, the 3NP conversion rate increases 36–38 times compared to the commercial material (Table S1†). Compared to the photocurrent measurements, where the activity improved with the increase of the {110} surface, the photocatalytic activity of reduction reactions enhances for crystals with a larger surface of the reductive {001} facets. Therefore, to achieve a high photocatalytic activity in the reduction of nitroaromatics, not only effective charge separation is needed, but also the availability of reductive {001} facets should be provided. Cyclic tests were also performed on cubes and truncated rhombic dodecahedrons in the reduction reaction of 1-iodo-4-nitrobenzene (Fig. S8†). The materials retained their photocatalytic activity.

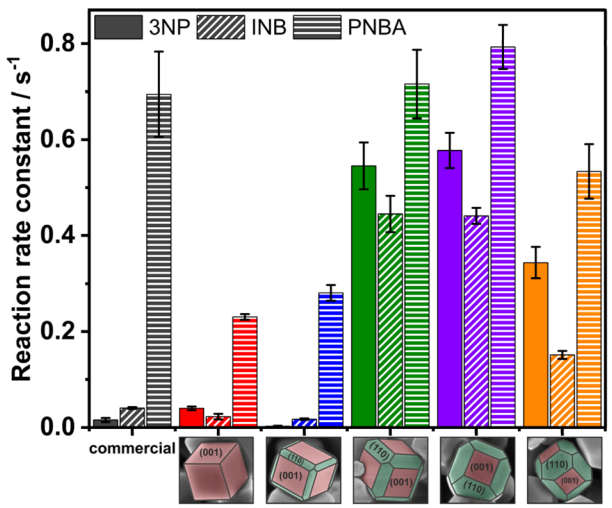

Fig. 6 Reaction rate constants for 3-NP, INB and PNBA reduction reaction in the presence of commercial and tailored $SrTiO_3$ crystals.

Conclusions

In this work, a series of $SrTiO_3$ crystals with a systematic morphology evolution were successfully synthesised using alcohols with different pK_a values. The obtained five materials are uniform and differ only in the shape, type of the exposed facets and their ratio. Based on the photoelectrochemical measurements, photodeposition experiments and oxidation of terephthalic acid, it was proven that reduction reactions occur preferably on the {001} facets, while oxidation reactions take place predominantly on the {110} facets. Additionally, a second type of facets, {110}, plays a crucial role in enhancing charge separation, significantly contributing to improved photocatalytic activity. Overall, the photocatalytic activity was higher for rhombic dodecahedrons with two types of facets. The reduction of three nitroaromatic compounds was successfully achieved with high efficiency using tailored $SrTiO_3$. This remarkable photocatalytic performance of the modified $SrTiO_3$ crystals is attributed to the synergistic effects of enhanced charge separation and the presence of the reductive {001} facets. The presented study is the first example of the selective photocatalytic reduction of nitroaromatics to amines on $SrTiO_3$. Moreover, the systematic analysis elucidates the role of particular facets in reduction and oxidation counterparts.

Data availability

The data supporting this article have been included as part of the ESI† and will also be available in the Cracow Open Research Data Repository (https://www.uj.rodbuk.pl/).

Author contributions

Wiktoria Adamowicz: Investigation, methodology, validation, visualization, writing – original draft, writing – review & editing; Wojciech Macyk: Funding acquisition, methodology, project

administration, resources, supervision, writing – original draft, writing – review & editing; Marcin Kobielusz: Conceptualization, funding acquisition, investigation, methodology, supervision, writing – original draft, writing – review & editing.

Conflicts of interest

There are no conflicts to declare.

Acknowledgements

The authors acknowledge the support of the National Science Centre within the OPUS23 project (2022/45/B/ST5/04087) and the Faculty of Chemistry under the Strategic Programme Excellence Initiative at Jagiellonian University. The study was carried out using research infrastructure funded by the European Union in the framework of the Smart Growth Operational Programme, Measure 4.2; Grant No. POIR.04.02.00-00-D001/20, "ATOMIN 2.0 – Center for materials research on ATOMic scale for the INnovative economy". The authors thank Dr Kaja Spilarewicz for SEM and EDS measurements.

References

1 S. Wang, S. Li, H. Feng, W. Yang and Y.-S. Feng, *ACS Appl. Mater. Interfaces*, 2023, **15**, 4845–4856.
2 H. Hirakawa, M. Katayama, Y. Shiraishi, H. Sakamoto, K. Wang, B. Ohtani, S. Ichikawa, S. Tanaka and T. Hirai, *ACS Appl. Mater. Interfaces*, 2015, **7**, 3797–3806.
3 S. Gisbertz and B. Pieber, *ChemPhotoChem*, 2020, **4**, 456–475.
4 W. Adamowicz, K. Yaemsunthorn, M. Kobielusz and W. Macyk, *ChemPlusChem*, 2024, e202400171.
5 D. Franchi and Z. Amara, *ACS Sustain. Chem. Eng.*, 2020, **8**, 15405–15429.
6 C. Avcıoğlu, S. Avcıoğlu, M. F. Bekheet and A. Gurlo, *ACS Appl. Energy Mater.*, 2023, **6**, 1134–1154.
7 B. L. Phoon, C. W. Lai, J. C. Juan, P.-L. Show and G.-T. Pan, *Int. J. Hydrogen Energy*, 2019, **44**, 14316–14340.
8 R. Li, T. Takata, B. Zhang, C. Feng, Q. Wu, C. Cui, Z. Zhang, K. Domen and Y. Li, *Angew. Chem., Int. Ed.*, 2023, **135**, e202313537.
9 Z. Pan, J. J. M. Vequizo, H. Yoshida, J. Li, X. Zheng, C. Chu, Q. Wang, M. Cai, S. Sun and K. Katayama, *Angew. Chem.*, 2024, e202414628.
10 Y. Qin, F. Fang, Z. Xie, H. Lin, K. Zhang, X. Yu and K. Chang, *ACS Catal.*, 2021, **11**, 11429–11439.
11 Z. Zhao, E. J. Willard, H. Li, Z. Wu, R. H. Castro and F. E. Osterloh, *J. Mater. Chem. A*, 2018, **6**, 16170–16176.
12 Z. Zhao, R. V. Goncalves, S. K. Barman, E. J. Willard, E. Byle, R. Perry, Z. Wu, M. N. Huda, A. J. Moulé and F. E. Osterloh, *Energy Environ. Sci.*, 2019, **12**, 1385–1395.
13 K. M. Macounová, R. Nebel, M. Klusáčková, M. Klementová and P. Krtil, *ACS Appl. Mater. Interfaces*, 2019, **11**, 16506–16516.
14 T. Takata, J. Jiang, Y. Sakata, M. Nakabayashi, N. Shibata, V. Nandal, K. Seki, T. Hisatomi and K. Domen, *Nature*, 2020, **581**, 411–414.
15 J.-i. Fujisawa, T. Eda and M. Hanaya, *Chem. Phys. Lett.*, 2017, **685**, 23–26.
16 Y. Li, H. Li, S. Le, X. Bai and X. Wang, *J. Cleaner Prod.*, 2020, **245**, 118919.
17 A. Shawky, M. Alhaddad, K. Al-Namshah, R. Mohamed and N. S. Awwad, *J. Mol. Liq.*, 2020, **304**, 112704.
18 X.-M. Cheng, J. Zhao and W.-Y. Sun, *EnergyChem*, 2022, **4**, 100084.
19 Y.-K. Peng and S. E. Tsang, *Nano Today*, 2018, **18**, 15–34.
20 X. Han, E. Zarkadoula, Q. Huang, M. L. Crespillo, X. Wang and P. Liu, *Nano Today*, 2022, **46**, 101612.
21 L. Dong, H. Shi, K. Cheng, Q. Wang, W. Weng and W. Han, *Nano Res.*, 2014, **7**, 1311–1318.
22 L. Mu, Y. Zhao, A. Li, S. Wang, Z. Wang, J. Yang, Y. Wang, T. Liu, R. Chen and J. Zhu, *Energy Environ. Sci.*, 2016, **9**, 2463–2469.
23 Q. Jia, J. Liu, L. Zhong, Y. Li and D. Duan, *Mater. Lett.*, 2021, **288**, 129338.
24 B. Wang, S. Shen and L. Guo, *Appl. Catal., B*, 2015, **166**, 320–326.
25 T. Kimijima, K. Kanie, M. Nakaya and A. Muramatsu, *Appl. Catal., B*, 2014, **144**, 462–467.
26 S. Assavachin, C. Xiao, K. Becker and F. E. Osterloh, *Energy Environ. Sci.*, 2024, **17**, 3493–3502.
27 Y. Zhang, X. Wu, Z.-H. Wang, Y. Peng, Y. Liu, S. Yang, C. Sun, X. Xu, X. Zhang and J. Kang, *J. Am. Chem. Soc.*, 2024, **146**, 6618–6627.
28 Q. Shen, W. Kang, L. Ma, Z. Sun, B. Jin, H. Li, Y. Miao, H. Jia and J. Xue, *Chem. Eng. J.*, 2023, **478**, 147338.
29 G. S. Foo, Z. D. Hood and Z. Wu, *ACS Catal.*, 2018, **8**, 555–565.
30 Z. Bao, V. Fung, F. Polo-Garzon, Z. D. Hood, S. Cao, M. Chi, L. Bai, D.-e. Jiang and Z. Wu, *J. Catal.*, 2020, **384**, 49–60.
31 P.-L. Hsieh, G. Naresh, Y.-S. Huang, C.-W. Tsao, Y.-J. Hsu, L.-J. Chen and M. H. Huang, *J. Phys. Chem. C*, 2019, **123**, 13664–13671.
32 B. Wang, S. Shen and L. Guo, *ChemCatChem*, 2016, **8**, 798–804.
33 A. Vijay and S. Vaidya, *ACS Appl. Nano Mater.*, 2021, **4**, 3406–3415.
34 C. Wang, Y. Li, X. Cai, D. Duan and Q. Jia, *J. Mater. Chem. A*, 2023, **11**, 21046–21057.
35 B. Wang, B. An, X. Li and S. Shen, *Front. Energy*, 2024, **18**, 101–109.
36 J. Ling, K. Wang, Z. Wang, H. Huang and G. Zhang, *Ultrason. Sonochem.*, 2020, **61**, 104819.
37 P.-L. Hsieh, M. Madasu, C.-H. Hsiao, Y.-W. Peng, L.-J. Chen and M. H. Huang, *J. Phys. Chem. C*, 2021, **125**, 10051–10056.
38 L. Mu, B. Zeng, X. Tao, Y. Zhao and C. Li, *J. Phys. Chem. Lett.*, 2019, **10**, 1212–1216.
39 Q. Jia, C. Wang, J. Liu, X. Cai, L. Zhong, G. Yu and D. Duan, *Nanoscale*, 2022, **14**, 12875–12884.
40 J. Yan, Z. Wei, W. Fang, J. Chi, H. Luo, Z. Jiang, C. Terashima and W. Shangguan, *ACS Appl. Nano Mater.*, 2025, **8**(9), 4553–4564.
41 P. Makuła, M. Pacia and W. Macyk, *J. Phys. Chem. Lett.*, 2018, **9**, 6814–6817.

42 K. Yaemsunthorn, M. Kobielusz and W. Macyk, *Catal. Today*, 2024, **432**, 114598.
43 L. Chang, S.-T. Yong, S.-P. Chai, L. Putri, L.-L. Tan and A. Mohamed, *Mater. Today Chem.*, 2023, **27**, 101334.
44 G. Kumar, Z.-L. Chen, S. Jena and M. H. Huang, *J. Mater. Chem. C*, 2023, **11**, 3885–3888.
45 G. Žerjav, A. Albreht, I. Vovk and A. Pintar, *Appl. Catal., A*, 2020, **598**, 117566.
46 J. Kong, Z. Rui and H. Ji, *Ind. Eng. Chem. Res.*, 2016, **55**, 11923–11930.
47 Z. Wang, X. Hao, S. Gerhold, Z. Novotny, C. Franchini, E. McDermott, K. Schulte, M. Schmid and U. Diebold, *J. Phys. Chem. C*, 2013, **117**, 26060–26069.
48 W. Gong, X. Liu, D. Gao, Y. Yu, W. Fu, D. Cheng, B. Cui and J. Bai, *Chemosphere*, 2015, **119**, 835–840.
49 P. Eskandari, F. Kazemi and Z. Zand, *J. Photochem. Photobiol., A*, 2014, **274**, 7–12.
50 D. Formenti, F. Ferretti, F. K. Scharnagl and M. Beller, *Chem. Rev.*, 2018, **119**, 2611–2680.